Published in final edited form as:

Sci Transl Med. 2022 January 19; 14(628): eabj1441. doi:10.1126/scitranslmed.abj1441.

Human Brain Mapping with Multi-Thousand Channel PtNRGrids Resolves Spatiotemporal Dynamics

Youngbin Tchoe[1,†], **Andrew M. Bourhis**[1,†], **Daniel R. Cleary**[1,2,†], **Brittany Stedelin**[3], **Jihwan Lee**[1], **Karen J. Tonsfeldt**[1,4], **Erik C. Brown**[3], **Dominic Siler**[3], **Angelique C. Paulk**[5], **Jimmy C. Yang**[5,6], **Hongseok Oh**[1], **Yun Goo Ro**[1], **Keundong Lee**[1], **Samantha Russman**[1], **Mehran Ganji**[1], **Ian Galton**[1], **Sharona Ben-Haim**[1,2], **Ahmed M. Raslan**[3], **Shadi A. Dayeh**[1,2,7,*]

[1]Integrated Electronics and Biointerfaces Laboratory, Department of Electrical and Computer Engineering, University of California San Diego, La Jolla, California 92093, United States

[2]Department of Neurological Surgery, University of California San Diego, La Jolla, California 92093, United States

[3]Department of Neurological Surgery, Oregon Health & Science University, Mail code CH8N, 3303 SW Bond Avenue, Portland, Oregon 97239-3098, United States

[4]Department of Obstetrics, Gynecology, and Reproductive Sciences, Center for Reproductive Science and Medicine, University of California San Diego, La Jolla, California 92093, United States

[5]Department of Neurology, Massachusetts General Hospital, Boston, Massachusetts 02114, United States

[6]Department of Neurosurgery, Massachusetts General Hospital, Boston, Massachusetts 02114, United States

[7]Graduate Program of Materials Science and Engineering, University of California San Diego, La Jolla, California 92093, United States

Abstract

Electrophysiological devices are critical for mapping eloquent and diseased brain regions and for therapeutic neuromodulation in clinical settings and are extensively utilized for research in brain-machine interfaces. However, the existing clinical and experimental devices are often limited in either spatial resolution or cortical coverage. Here, we developed scalable manufacturing processes with a dense electrical connection scheme to achieve reconfigurable thin-film, multi-thousand channel neurophysiological recording grids using platinum-nanorods (PtNRGrids). With

*Corresponding author. sdayeh@eng.ucsd.edu.
†These authors contributed equally to this work

Author contributions: S.A.D. conceived and led the project. Y.T. fabricated the PtNRGrids, designed the tasks, and conducted all data analysis with S.A.D.'s guidance. A.M.B. designed the custom-made acquisition system and the motor task and stim-capture hardware with input from I.G. and participated in data analysis; D.R.C., B.S., D.S., A.C.P., J.Y., S.B-H. and A.M.R. performed tests and guided the electrode design for clinical translation. Y.T., A.M.B., K.L., K.J.T. performed the rat experiments and K.J.T. performed the histology. B.S., E.B, and A.M.R. designed clinical experiments and performed OR recordings; D.R.C., D.S., Y.T., A.M.B., and S.R. participated in some of the OR recordings. J.L. fabricated PtNRGrids used in the sensory/motor tasks and Y.G.R., and M.G. contributed to the fabrication process development. H.O. performed the bending cycle tests. A.C.P. and Y.T. composed the videos on the reconstructed brain models of subjects from fMRI and structural MRI. S.A.D. and Y.T. wrote the manuscript and all authors discussed the results and contributed to the manuscript writing.

PtNRGrids, we have achieved a multi-thousand channel array of small (30 μm) contacts with low impedance, providing high spatial and temporal resolution over a large cortical area. We demonstrated that PtNRGrids can resolve sub-millimeter functional organization of the barrel cortex in anesthetized rats that captured the tissue structure. In the clinical setting, PtNRGrids resolved fine, complex temporal dynamics from the cortical surface in an awake human patient performing grasping tasks. Additionally, the PtNRGrids identified the spatial spread and dynamics of epileptic discharges in a patient undergoing epilepsy surgery at 1 mm spatial resolution, including activity induced by direct electrical stimulation. Collectively, these findings demonstrated the power of the PtNRGrids to transform clinical mapping and research with brain-machine interfaces.

One Sentence Summary:

PtNRGrids offer high spatial resolution and cortical coverage and reveal functional organization and neuronal dynamics.

INTRODUCTION

Functional mapping with direct electrical stimulation paired with neurophysiological recording is the gold standard for mapping the human brain and delineating the margins between functional and pathological tissue(1–4). Neurophysiological recording with non-penetrating surface electrocorticography (ECoG) grids have been used for over six decades to attain reliable clinical information and improve patient outcomes during surgical interventions(3, 4). ECoG grids can have cortical coverage of up to 8×8 cm^2 and interelectrode pitch as small as 4 mm(2, 5–10). Higher resolution grid such as the penetrating Utah arrays have less coverage (4×4 mm^2) and better pitch (0.4 mm) than ECoG grids but require invasive surgery to be implanted in deep brain areas (1, 11–14). These are the de facto standard for research on chronic neural prostheses for motor control and decoding language, as well as for providing sensory feedback in paraplegic individuals via closed loop devices(5–10, 12, 15–23). Although great progress has been made using these devices, the next steps in neuroprostheses and neural decoding requires higher spatial resolution(24–26) and expanded coverage of the cortex.

We used advanced thin-film microfabrication techniques and a biocompatible platinum nanorod (PtNR)(27) microelectrode material to develop large surface-area ECoG grids with both high resolution and broad spatial coverage. Our PtNRGrids are built on thin, conformal parylene C substrates, and the distribution of contacts is reconfigurable for different pitches and area coverage. We utilized compact one-touch connectors to enable a simple and reliable interface with thousands of channels that is amenable to the constraints of the operating room. Here, we demonstrated the use of these PtNRGrids to isolate submillimeter functional boundaries of individual cortical columns in controlled animal experiments, and neural mapping from both awake and anesthetized patients undergoing tumor or epileptogenic tissue resection.

RESULTS

Fabrication of Multi-Thousand Channel PtNRGrids and Connectorization

PtNRGrids were composed of contacts embedded in flexible sheets of 6.6 μm thick parylene C, specially designed for recording neural activity on the cortical surface (Fig. 1). The layout, shape, and size of the PtNRGrids were generated with customizable designs by leveraging established microelectromechanical systems (MEMS) fabrication techniques on large 18 × 18 cm^2 glass wafers and a newly developed, biocompatible PtNR(27) microelectrode material. This process produced multiple 17 cm long and up to 8 × 8 cm^2 large area coverage electrodes ranging from 1024 to 2048 electrode contacts or channels with high uniformity and yield (Fig. 1). The 30 μm wide PtNR contacts were recessed by ~2 μm below the surface of parylene C to prevent shear forces on PtNRs during implant (Fig. 1B;(27)). Between the PtNR contacts and the bond pads, we routed gold traces which were 500 nm thick, 4 μm wide, 6 μm apart, and over 10 cm long, and fully encapsulated between two layers of parylene C (3.5 μm bottom and 3.1 μm top, Fig. S1, S2). We patterned perforation holes in the parylene C throughout the thin grid to perfuse saline and cerebrospinal fluid away from the electrode contacts. Therefore, an intimate interface between the PtNRGrids and the surface of the brain was maintained and electrochemical shunting between nearby recording contacts was avoided (Fig. S3). Additionally, the large-perfusion holes with diameters of 0.5 mm (Fig. 1C) and 0.9 mm (Fig. 1D) distributed across the grid provided access for probes of a handheld clinical stimulator to directly stimulate any point of the cortex through the grid. We varied the pitch/coverage of the 30 μm PtNR contacts from 150 μm/5 × 5 mm^2 for rodent brain mapping (Fig. 1B) to 200 μm/3 × 13 mm^2 (Fig. 1E), 1 mm/32 × 32 mm^2 (Fig. 1C), and 1.8 mm/80 × 80 mm^2 (Fig. 1D) for human brain mapping. The detailed fabrication process of the PtNRGrids can be found in the supplementary materials. The fabrication process of multi-thousand channel PtNRGrids is also compatible with poly(2,3-dihydrothieno-1,4-dioxin)-poly(styrenesulfonate) (PEDOT:PSS) (Fig. S4).

A major bottleneck for scaling microelectrode arrays towards hundreds or thousands of channels was the connectorization of electrodes to acquisition circuits. Inspired by solutions used in the microelectronics industry which can reliably route high bandwidth connections to thousands of channels(28, 29), we utilized an off-the-shelf land grid array (LGA) – LGA1155 CPU socket – that was originally designed for the Intel's Sandy Bridge computer processors. Manufacturing the grids on large-area substrates ensures sufficient space to bond the PtNRGrids to custom LGA- printed circuit boards that mate with the LGA1155 socket without compromising the large area coverage of PtNRGrids or their long thin-film metal leads (Fig. 1D). An additional extender board was used to further increase the separation between the surgical field and a custom-acquisition board (Fig. S5), and for improved intraoperative handling procedures. The acquisition board connects to a 1024-channel electrophysiology control system, provided by Intan Technologies LLC (Fig. S6). The entire PtNRGrid and connector (Fig. 1C) were compatible with the conventional processes(30) used to sterilize surgical equipment, maintaining contact yields up to 99.4% with a narrow 1 kHz impedance distribution centered at 11 kΩ with a standard deviation of 2 kΩ (Figs. 1E–F), achieved with manual bonding of the electrodes to the printed circuit board (PCB)

(Fig. S3). The 1 kHz impedance magnitude, averaged over seven different PtNRGrids used in successful human recording experiments, was 10 ± 2 kΩ. The scalable process allowed us to obtain up to 95.2% contact yield with impedances ≤ 100 kΩ even when the total channel count increased to 2048 (Fig. 1F). The simple, one-touch connector methodology enabled our neurosurgical and research team to swiftly and reliably connect thousands of channels to the acquisition board across the boundary between the sterile and non-sterile zones. As a result, sterilization was limited to the disposable grid and its connector eliminating the need to sterilize the acquisition electronics. The setup allowed us to record simultaneously from 1024 channels with a sampling rate of 20,000 samples/second, thereby capturing full broadband neurophysiological activity.

The measured parasitic capacitance between neighboring channels on the PtNRGrids showed 10 million times higher impedance at 1kHz than the electrochemical impedance, resulting in −60dB crosstalk estimated by our measurements and simulations (see Figs. S7–S12). The PtNRGrids also exhibited mechanical stability exceeding the American National Standards Institute / Association for the Advancement of Medical Instrumentation ANSI/AAMI CI86:2019 recommendations (Fig. S13).

PtNRGrids Isolate Functional Cortical Columns from the Surface of the Brain

To test the broadband and high-resolution recording capabilities of the PtNRGrids, we mapped the primary somatosensory cortex of anesthetized rats. The rat cortex has well-defined organization of the somatosensory cortical structures, especially around the barrel cortex, where a series of sensory cortical columns map one-to-one with the whiskers.(31, 32) A square-shaped 1024 channel PtNRGrid with 150 μm pitch (Fig. 1B) was implanted to record from the entire right primary somatosensory barrel cortex (Fig. 2). To evoke sensory activity, air-puffs were delivered through a microcapillary tube to individually stimulate the contralateral-side whiskers. (Fig. 2A; Fig. S14). We consistently observed large-amplitude raw evoked responses (N=50) for whisker (E4) stimulation (Fig. 2B). The raw waveforms exhibit localized, high amplitude responses as large as 500 μV with peak responses observed ~30 ms after the onset of the air-puff (Fig. 2C). These responses propagated as traveling waves across the cortical surface (Fig. S15). The spatial localization of individual stimuli is best represented in the gamma band (30–190 Hz), as expected, and observed in the root-mean-square (RMS) power of the measured responses when bandpass filtered (Fig. 2D). The high-gamma activity (HGA; 70–190 Hz) is known to be highly correlated to the location and timing of cortical activation with a strong link to spiking activities,(33) so we used HGA to map functional boundaries of the rat barrel cortex (Fig. 2E). We observed clearly distinguishable submillimeter sensory boundaries that classified the responses to different whisker rows and columns, revealing spatially organized barrels with high spatial resolution. The locations of sensory-responsive areas were also identified by evoking cortical responses with air-puff stimulation of the neck, trunk and tail, and by electrical stimulation of the forepaw and hindpaw (Fig. 2E). The detailed signal processing procedures for HGA mapping (Figs. S16–S19) and the results across different rats (n = 4) could be found in the supplementary material (Fig. S20). Following completion of functional mapping, the implanted area was marked, and histochemical analyses were used to examine the anatomy under the implant.

The anatomical and functional boundaries were in agreement, as outlined using the vesicular-glutamate transporter 2 (VGLUT2), a well-established marker of thalamocortical afferents that compose the homunculus, including the barrels (Fig. 2F)(34). The localized HGA responses to whisker stimuli agree remarkably well to the VGLUT2-labeled positions of the barrels as well as the homunculus-labeled positions of the forelimb, hindlimb, neck, trunk, and tail (Fig. 2G). Thus, this single-grid based mapping provides a reliable real-time high-resolution functional mapping of the rat brain, which contrasts with the traditional serial probing while recording evoked responses(35, 36).

PtNRGrids Resolve the Curvilinear Nature of the Human M1-S1 Functional Boundary

Precise intraoperative localization of the central sulcus, the boundary between primary somatomotor (M1) and somatosensory (S1) cortices is a necessary approach in several neurosurgical procedures, particularly in the resection of tumors. This anatomical boundary is identified by a functional phase reversal of somatosensory evoked potentials (SSEPs) at the boundary between M1 and S1(37, 38), an a priori assumed anatomico-functional relationship. Most commonly, these SSEPs – recorded in response to electrical stimulation pulses to the peripheral nerves – are evoked 20 ms post stimulus and demonstrate opposite polarity in their potentials across this boundary. The presence of pathological tissue can induce a shift in the functional organization and location far from its presumed anatomical localization(39, 40), and make traditional sulcal markers harder to discern with low spatial resolution of clinical ECoG grids.

We recorded SSEPs from awake subjects (n = 4) undergoing tumor resection, each with a 1024-channel PtNRGrid with 1 mm spacing (Fig. 1C) placed across the central sulcus near the hand region of somatomotor sensory cortex while peripheral nerves were stimulated (Fig. 3A, 3D; Figs. S21–S22). The implantation site of the PtNRGrid was marked and identified on a reconstructed model of the patient's brain along with lesion location based on functional magnetic resonance imaging (fMRI) and structural MRI (Fig 3A). We observed a small stimulus artifact from peripheral nerve stimulation which was followed by high amplitude SSEPs 10~40 ms (Fig. 3B). These waveforms revealed characteristic positive and negative peaks(41) that reversed phase at the functional boundary (FB) denoting the M1-S1 functional boundary (Fig 3B, Fig. S23). Similar SSEP waveforms were recorded with a conventional dual column 2 × 8, 16-channel clinical ECoG grid with 10 mm spacing and 2.3 mm diameter recording contacts (Fig. 3C, Fig. S24–25). The maximum interpeak amplitude of SSEPs measured by the PtNRGrid was 214 μV (Fig. 3B), whereas SSEPs measured by the clinical ECoG grid (Fig. 3C) on the same patient only showed 5 μV interpeak amplitude.

The PtNRGrids revealed the precise curvilinear nature of the M1-S1 FB with millimeter scale resolution at a sampling frequency of 20 kHz. The subject's lesion (Fig. 3A) contributed to broadening and distorting the SSEP waveforms on both the PtNRGrids (Fig. 3B) and on the clinical ECoG (Fig. 3C), in agreement with the findings of prior clinical studies(37). Additionally, the SSEPs recorded with the PtNRGrid were minimally affected by the presence of underlying surface blood vessels ('CS' denoting the anatomical central sulcus in Fig. 3B) (42). Although the SSEPs were minimally affected by the blood vessel (Fig. S26), it is reported that higher frequency signals (30–70 Hz) could be attenuated by

30–40% by the presence of the blood vessel (42). To construct the two-dimensional maps for the curvilinear FB, we utilized the conventional potential-based phase reversal technique (Fig. 3E) and a correlation technique that we devised to identify the FB in diseased tissue (Fig. 3F). We calculated the Pearson correlation coefficients of the waveforms between 5 to 50 ms post-stimulus for all the working channels with respect to the channel in the middle of the grid. Channels with correlation coefficients above or below 0.5 were separated by a dotted line to depict the M1-S1 FB (Fig. 3F), which agrees well with that deduced directly from potential maps (Fig. 3E). We observed a highly detailed spatial map depicting considerable offset, based on SSEPs (Fig. 3) and HGA (Fig. 4), between the M1-S1 FB and the anatomical central sulcus using the PtNRGrid (FB versus CS in Fig. 3D), consistent with functional reorganization with brain lesions.(39, 40). However, it is important to note that these SSEPs are projections of event related potentials (ERPs) from deeper layers that are often oblique to the plane of the cortical surface. Extension of this functional boundary below the surface must be validated with depth recordings(43). Nevertheless, the M1-S1 FB revealed by the PtNRGrid was concordant with the gold standard clinical mapping using conventional bipolar stimulation, and with higher resolution than conventional clinical ECoG grid passive gamma mapping using CortiQ system.

We also recorded SSEPs from the human brain using 2048 channel PtNRGrid with 1.8 mm pitch (Fig. 1D, Figs. S27–S29). The waveforms (30–3000 Hz, N=22) exhibit clear P20-N20 peaks responses ~20 ms after the median nerve stimulation (Fig. 3G). The severe anatomical distortion and the limited time of recording precluded assessing a functional boundary in this return surgery (Fig. S30). Nevertheless, the results of Fig. 3G illustrate that the scalable PtNRGrids enable multithousand channel recordings from the human brain.

1024 channel PEDOT:PSS electrodes with 1 mm pitch and 100 μm electrode contact diameter also recorded SSEPs from the human brain with an interpeak amplitude up to 57 μV (Fig. S31).

PtNRGrids Reveal Large Scale Spatiotemporal Dynamics of Motor and Sensory Activity in Humans

Motivated by the rise of interest in using ECoG grids for brain-machine interfaces(5, 8–10, 21–23), we investigated whether the high spatial and temporal resolution of the PtNRGrid could be used to map sensory- and motor-evoked activities. Following the phase reversal mapping of the functional M1-S1 boundary and with the same PtNRGrid placement on the same participant, we either stimulated individual fingers with vibrotactile stimulators, or asked the patient to perform specific hand movements (Fig. 4A; Fig. S32). Following individual fingertip stimulation, we observed a clear enhancement in HGA as large as 3 sigma (σ) from baseline (Fig. 4B), the largest of which were localized only in the primary somatosensory cortex (Fig. 4B). Vibrotactile stimulation of each fingertip evoked spatially distinctive HGA patterns, with some channels tuning to all fingertips with varying magnitudes. After superimposing HGA on an optical image of the implanted PtNRGrid, we could observe the fine spatial distribution of the neural correlates of vibrotactile stimulation and compare this with the M1-S1 boundary and the cortical anatomy using phase reversal (Fig. 4C).

We next demonstrated the high spatiotemporal capabilities of the PtNRGrids during a hand grasping task (Fig. 4D–L). As with the vibrotactile stimulation, we observed highly localized HGA on the PtNRGrid during the motion (Fig. 4G), near completion of motion (Fig. 4H), and for 100 ms after completion of motion (Fig. 4I) (See also Movie S1). Furthermore, coordination between the S1 and M1 cortices during the grasping task could be seen at high resolution via the PtNRGrid. In a snapshot of the dynamics through time along a single line of electrodes cut across a corner of the grid (highlighted by the yellow rectangle in Fig. 4I), we illustrate the spatial dynamics for the selected 16 channels across the M1-S1 boundary for the high gamma (HG) (Fig. 4E) and beta (Fig. 4F) bands. These band-specific (spectrotemporal) dynamics showed remarkable correlation with the hand movement captured by time-locked flex sensors on the subject's hand (Fig. 4D). Distinctive HGA in the M1 cortex was observed during motor initiation, was seen in both M1 and S1 cortex during the hand closure onset, and finally, lingered only within the S1 cortex when motion was complete. High amplitude beta wave in the M1 cortex was observed prior to the motion, during the planning stage, attenuated during execution of the motion, and increased once again after the motion was completed (Fig. 4D–F). Similar behavior was observed under trials of repeated hand grabbing motion (see Figs. S33). These observations of alternating amplitude in HG and beta activity before, during, and after the motion agree with prior observations(44–46).

Lastly, we showed that with the large channel count of the PtNRGrid, we could construct maps of brain wave propagation at high spatial resolution within a physiologically relevant cortical coverage (Figs. 4J–L, Fig S34). During the hand grasping task, we calculated the spatial gradient of the phase of the beta waves(47, 48) recorded by our PtNRGrids to infer propagation direction (Figs. 4J–L, Figs. S35–S38 and Movies S2–S3). We further overlaid streamlines originating from selected regions in S1 and M1 cortices on top of the vector fields for a visual aid of the long-range propagation directions. We found clear propagation dynamics across the M1-S1 FB which correlated with the hand grabbing motion. In the preparation stage of the motion, we observed noticeable long range beta waves propagating from the S1 cortex to M1 cortex (Fig. 4J). During the motion, the beta waves were suppressed and exhibited lack of coherence in the vector fields (Fig. 4K). After the motion was complete, the propagating direction reversed, as represented by the streamlines (Fig. 4L, atop a reconstructed brain model in Movie S4). By detecting propagation dynamics of beta waves with high spatial resolution at physiologically relevant coverage using our PtNRGrids, we have enhanced functional mapping by revealing large-scale brain activity across frequency bands.

PtNRGrids Record Pathological Wave Dynamics

Finally, we determined the utility of PtNRGrids for high-resolution intraoperative neuromonitoring to detect ictal onset zones and patterns of seizure spread. PtNRGrids (1 mm spacing, 32 × 32 contacts, 0.5 mm diameter perfusion holes (Fig. 1C)) were placed over the cortex in a patient with intractable epilepsy related to a left anterior temporal lobe cavernoma who elected for surgical resection (Fig. 5A). Using PtNRGrids allowed passive recordings of local field potential (LFP) as well as active electrical stimulation through the perfusion holes (uniformly distributed at 0.5 mm diameter, 1 mm spaced, Fig. 5A) using a

standard handheld clinical stimulator (Fig. 5A) to induce interictal epileptiform activity(49–52). Control benchtop experiments on brain models made of gelatin confirmed that the PtNRGrid electrode and the electronics were not affected by the bipolar stimulation (Fig. S39).

Passive mapping of the epileptogenic tissue with the PtNRGrid revealed ongoing epileptiform activity (Fig. 5B–F), also shown in the spatial mapping of RMS amplitude of the neural activity filtered in the frequency window of 10 to 59 Hz at different time epochs (Fig. 5E). The onset of epileptiform activity began near the lower right corner of the grid, then spread across the vertical midline, and terminated at the lower left corner (Fig. 5B and Movie S5). To investigate whether the observed epileptiform waves were consistent over time, we applied automatic detection algorithms, generally used for detecting interictal discharges(53), to all channels and generated a raster plot of the activity as a function of time (Fig. 5D, F). After sorting the channels according to the distance from the lower right corner, we found a 20 s window with repetitive epileptiform events occurring approximately every 4 s across the entire grid (Fig. 5F), which is magnified to show a single event of a recurring epileptiform waveform within a 4 s time window (Fig. 5D, Fig. 5E). These repeated epileptiform waves consistently originated from the lower right corner of the grid, spread across the entire grid within one second, and subsequently disappeared one second later. Automatically detected epileptiform events (Fig. 5E) exhibit clear temporal shifts between the spontaneous epileptiform waveforms from channel to channel (overlayed on a reconstructed brain model of the participant in Movie S6). Collectively, these maps and videos provide further evidence of utility for the PtNRGrids for large-scale high-resolution mapping of such pathologic activity.

Active mapping was performed in the same patient (Figs. 5G–M). Utilizing the same epileptiform discharge detection algorithm as Fig. 5D, we counted the number of channels on the PtNRGrid that detected epileptiform discharges and plotted the number of events as a function of time (Fig. 5H). Spontaneous and repetitive epileptiform activity persisted across the entire recording. Regardless of the stimulation location, we observed that stimulation pulses with short duration (< 1 s) did not increase the underlying spontaneous epileptiform discharge activity (Fig. 5I). However, longer stimulation trials of 1.4 – 1.9 s such as trials 4, 5, and 6 significantly increased the number of epileptiform discharge events ($p < 0.001$) for the recording channels within 16 mm from the stimulation point (N = 471, 199, and 304 for trials 4, 5, and 6, respectively), particularly events with characteristics similar to interictal discharges. The duration of the pulse determines the total delivered charge density that is correlated with evoked responses(54, 55). The spatially resolved heatmaps of the stimulation evoked activity can be clearly observed where it can be noted that the longer trials (4 and 6) were characterized by significantly enhanced after-discharges detected around the stimulation positions ($p < 0.001$) (Fig. 5I).

In stimulation-evoked epileptiform discharges, we found a clear enhancement of the amplitude of detected epileptiform activity within the 10–59 Hz frequency window which persisted for more than 5 s after the bipolar stimulation ceased (Fig. 5J; see also Movie S7). By sorting the automatically detected epileptiform events according to distance from the stimulation center (Fig. 5L), we observed that the first epileptiform events were

initiated near the stimulated region. Following stimulation, bursts of epileptiform discharges occurred every 0.3 s and continued for a longer duration than the less frequent spontaneous epileptiform discharges. These phenomena are clearly exhibited in the raw waveform recordings from selected channels (Fig. 5L, M), and can be viewed atop a reconstructed brain model of the participant (Movie S8).

Finally, we investigated the origin and spatiotemporal dynamics of both the spontaneous and stimulation-induced epileptiform activity using vector fields and streamlines. Immediately before epileptiform events, the vector fields are mostly incoherent (Figs. S40–S41), but become coherent near the larger amplitude epileptiform events. The characteristics of the spontaneous epileptiform activity can be inferred from the red streamlines that originate from the right lower corner near the location of the lesion in this patient (Fig. 5C). In contrast, the streamlines for stimulation-evoked epileptiform activity originate and spread away from the position of the stimulator (Fig. 5K), demonstrating high resolution spatial and temporal mapping of the sites of origin. The epileptogenic tissue tested by this experiment was removed as a planned left temporal lobectomy which included lesional (cavernoma) tissue and all the epileptic neocortical tissue discerned by prior sEEG seizure mapping and deemed resectable as well by the PtNRGrid. The patient remained seizure free to the date of this manuscript synthesis, which is approximately 6 months after surgery.

DISCUSSION

Our studies demonstrate the range of utility of PtNRGrids for high spatial and temporal recording of neural activity for research and clinical intraoperative use. The PtNRGrids were built on thin, transparent, and conformal substrates and were reconfigured in pitch and total cortical coverage with 1024 and 2048 low impedance contacts over an area as large as 8 × 8 cm^2, scalable for rodent or human work. The fabrication was performed on a large-area 180 mm × 180 mm glass substrate with thin film processes substantially advancing the manufacture of neural probes beyond the conventional 100 mm and 150 mm silicon (Si) substrates. The larger area manufacturing afforded the capability to connect to thousands of channels and the formation of long metal strips to isolate the sterile surgical medium from the acquisition electronics for patient safety. Additionally, the fabrication process afforded large area coverage of the PtNRGrids on the brain (up to 8 cm × 8 cm achieved in this work) and safety and sterility in the operating room for intraoperative monitoring purposes. Successful transition to the large-area glass substrates opens the possibility of integrating the display panel manufacturing technology with neurotechnology and promises excellent scalability considering the size of the glass panel used in display industry (up to few meters squared) and the high-resolution lithography capability (1.2 μm for both metal line and space (L/S)) of flat panel displays (56). The large area glass substrates also offer potential advances in manufacturing biomedical devices for use in humans which can leverage electronic (thin film transistors) and optoelectronic (light emitting diodes and imagers) advances achieved by the display industry for utility in human biomedical devices.

A commonly voiced concern over increasing the channel count of microelectrode arrays is the potential for electrical crosstalk to introduce artifacts into the neurophysiological recordings. This electrical crosstalk is primarily a result of parasitic capacitance between

neighboring leads and thus will scale directly with increasing trace length and inversely with their trace pitch. Thus, traces should be kept short to reduce these parasitic paths. The termination impedance of neighboring channels to tissue (the electrochemical interfacial impedance) also needs to be accounted for, especially for conventional high-impedance electrochemical interfaces which can affect crosstalk through parasitic capacitance paths. However, this is not a concern for the low impedance PtNR contacts which maintain 1 kHz impedances that are at least 10 million times lower than the impedance of the parasitic capacitances.

We show high-fidelity broadband recordings from rodents, where the high spatial resolution of the PtNRGrids enabled identification of individual cortical columns from the surface of the brain. The PtNRGrids were easily translated to the intraoperative setting, enabling the first human recordings with 1024 channel PtNRGrids from 13 subjects, and 2048 channel PtNRGrids from one subject. The PtNRGrids mapped sensory and pathological epileptiform activity from the surface of the brain, and detected relevant somatosensory dynamics in high spatial resolution over a physiologically relevant cortical coverage. Previous investigations of propagation characteristics of beta waves in the human brain were carried out with relatively small area coverage of $4 \times 4 mm^2$ using Utah arrays(47, 57), or with ECoG grids with sparse 1 cm spatial resolution(48).

The PtNRGrids revealed the precise curvilinear nature of the M1-S1 FB with millimeter scale resolution at a sampling frequency of 20 kHz, superior to the low-resolution boundaries identified with conventional ECoG grids (41) or the temporally limited fMRI (58). The SSEPs measured with PtNRGrids had interpeak amplitudes up to 214 μV, compared to the 5 μV interpeak amplitudes measured on the same patient with the clinical grid. It should be noted that interpeak amplitudes have been observed to fall within a range of 5 μV to 120 μV in a 230 patient study of clinical ECoG grid recordings (37). The lower amplitudes on the clinical grid can be attributed to both a spatial averaging on their ~6000X larger surface area than the PtNR contacts and a lower conformity to the brain surface resulting from the 1 mm thick substrate used in clinical grids (compared to the 6.6 μm thick parylene C substrate used in our PtNRGrids). It is also possible that the clinical ECoG grid that has sparsely distributed contacts (1 cm) missed the cortical region with the highest SSEP amplitude since it is a usual practice to adjust the location and angle of clinical ECoG grid to obtain maximum peak amplitude(37). We demonstrated high resolution recordings from the surface of the human brain with 1024 and 2048 channel PtNRGrids, which enables high resolution intraoperative recordings in neurosurgical operations, estimated to be as many as 13.8M annually.(59) However, the system in its current form does not enable chronic recordings, which have different design considerations that are beyond the scope of this work. To achieve chronic recordings, either denser custom-made connectors that are slim enough to be externalized through the scalp– as done in epilepsy monitoring – or direct integration of integrated circuits and wireless transceivers to the implant become necessary. (25, 60) The engineering challenges for each part of the implant increase and their safety as well as the durability of efficacy become critical.

We demonstrated recording density up to 4,444 cm^{-2} (contact pitch: 150 μm) using a single metallization layer of 10-μm-pitch metal leads and 30-μm-diameter PtNR contacts.

To increase the recording density, the width of the metal leads would need to decrease to enable tighter pitch and thickness would need to increase to maintain low metal lead impedance. There are practical lithographic limitations for patterning narrow and thick metal leads necessitating the use of multi-layer metallization which relaxes the constrains on the metal lead width. By making dual and triple layer electrodes, the electrode density can increase up to 17,776 cm^{-2} (contact pitch: 75 μm) and 71,104 cm^{-2} (contact pitch: 37.5 μm), respectively. Higher recording densities beyond 71,104 cm^{-2} would require a smaller PtNR contact diameter. A trade-off between the recording density and the impedance magnitude of the individual contacts will need to be considered.

The development of a real-time display of PtNRGrid recordings in a meaningful and potentially medically informative way holds the potential to improve surgical procedures. Although the higher resolution mapping can carry important implications for neurosurgical procedures, it is important to note that the surgical precision in current clinical practice does not meet mm-resolution. However, surgical resection boundaries obtained with current clinical electrodes are grossly determined with their 1 cm contact spacing. We anticipate that the PtNRGrids that determine surgical boundaries with mm-resolution might inform better resection practices by delineating the curvilinear nature of the functional and pathological boundaries that is not possible otherwise. With the development of higher-precision resection methods such as laser ablation or robot-assisted surgery, mm-scale spatial resolution recording might result useful for performing mm-scale resection of the brain tissue.

Lastly, the PtNRGrids were used for passive mapping in this work. Although the PtNRGrid has perfusion holes that enabled bipolar stimulation with external devices, direct current stimulation through the grid is desired. Additionally, micro-stimulation of smaller tissue volume may be preferred, particularly for individual functional cortical columns that were isolated using the PtNRGrids. Extension of this work should enable stimulation through the PtNRGrids which were shown in our earlier work to hold one of the highest charge injection capacities for safe stimulation(27).

PtNRGrids hold promise for superior mapping during neurosurgical intervention through high spatial resolution and coverage while maintaining excellent broadband temporal resolution compared to the clinical electrodes. PtNRGrid technology has the capacity to scale to more than 2048 channels and to pave the way for better neurosurgical mapping strategies, to enable possibilities for therapies, brain-computer interfaces, and better patient outcomes as the technology is advanced for chronic applications.

MATERIALS AND METHODS

Study design

Objectives of the study were to: (i) demonstrate that 1024 and 2048-channel PtNRGrids have higher spatial resolution that better delineated functional boundaries in the human brain than the standard clinical electrodes; (ii) test the signal amplitudes of PtNRGrids compared to the standard clinical electrodes; (iii) isolate the neural correlates and dynamic activity during motor and sensory tasks with high spatial resolution with the PtNRGrids; and

(iv) investigate the microscale dynamics of spontaneous and stimulation-evoked epileptic discharges with the PtNRGrids. All animal experiments were approved by the UCSD Institutional Animal Care and Use Committee (IACUC) under protocol S16020. We successfully gathered surface ECoG recordings of all intended stimulus-evoked responses and gathered post-mortem histological stains from two rats. These data were not blinded, and we did not include a randomization of subject selection in this study.

Twenty human subjects were recruited to participate in this study under two Institutional Review Board (IRB) approvals (UC San Diego IRB #181556, Oregon Health and Science University IRB #19099). Subjects were considered for recruitment if the details of their surgery coincided with a particular experimental paradigm, for example motor mapping experiments required patients with an exposure of the motor and sensorimotor cortex and required clinical motor mapping to be part of their normal clinical care. We selected the types of PtNRGrids and tasks depending on the location and size of the craniotomy determined by the clinical team. Participants were informed of the research and given time to understand the risks and benefits of participation prior to being asked for consent. Data from each participant was de-identified prior to analysis, and each experimental paradigm included controls for acquiring a baseline recording prior to or throughout the given recording period. Trial numbers within a given subject recording were determined based on a maximum recording time of 15 minutes in the OR setting along with the number of variables being swept. The data collected from subjects with severe brain tumor, low responsiveness due to age, anesthesia, or surgical procedures, or task-unrelated cortical exposure were excluded from the study. We did not include a randomization of subject selection in this study because patient data were considered separate datasets. Experimental conditions and a summary of all subjects are presented in Table S1.

Statistical analysis

All statistical comparisons were performed using nonparametric measures, so we did not test for normality. Spontaneous epileptiform discharge rates for each recording channel detected using automatic algorithms (53) were estimated from the 6 min baseline recording data. After-discharge rates induced by stimulation for all recording channels were estimated by taking a 4 s time window starting between 0.5 and 4.5s after each bi-polar stimulation. Sample sizes for each stimulation trial were the recording channels within a 16 mm radius from the bipolar stimulation site that also had electrochemical impedance below 100 kΩ at 1 kHz. Under these criteria, the number of channels (N) used in statistical analysis for each stimulation trial number (#) defined as $N_{\#}$ were as following: $N_1 = 351$, $N_2 = 177$, $N_3 = 540$, $N_4 = 471$, $N_5 = 199$, $N_6 = 304$, $N_7 = 299$, $N_8 = 365$, $N_9 = 252$, $N_{10} = 357$, $N_{11} = 631$, $N_{13} = 284$, and $N_{14} = 633$. For the selected channels, Wilcoxon signed rank test was used to analyze if the stimulation significantly increased the number of discharges compared to that of the spontaneous discharges. Stimulation trial 12 was excluded from the statistical analysis because of the short time window between trials 12 and 13.

Supplementary Material

Refer to Web version on PubMed Central for supplementary material.

Acknowledgements

The authors acknowledge insightful discussions with Prof. Eric Halgren of UC San Diego and Prof. Sydney Cash of Massachusetts General Hospital, and Prof. Anna Devor and Prof. Martin Thunemann of Boston University. The authors are grateful for the technical support from the nano3 cleanroom facilities at UC San Diego's Qualcomm Institute where the PtNRGrid fabrication was conducted. This work was performed in part at the San Diego Nanotechnology Infrastructure (SDNI) of UC San Diego, a member of the National Nanotechnology Coordinated Infrastructure, which is supported by the National Science Foundation (Grant ECCS1542148).

Funding

This work was supported by the National Institutes of Health Award No. NBIB DP2-EB029757 to S.A.D., NIH BRAIN Initiative R01NS123655-01 to S.A.D. and UG3NS123723-01 to S.A.D. and NIDA R01-DA050159 to S.A.D. and the National Science Foundation (NSF) Awards No. 1728497 to S.A.D. and CAREER No. 1351980 to S.A.D. and an NSF Graduate Research Fellowship Program No. DGE-1650112 to A.M.B. Any opinions, findings, and conclusions or recommendations expressed in this material are those of the author(s) and do not necessarily reflect the views of the funding agencies.

Competing Interests:

The authors declare the following competing interests. Y.T., A.M.R. and S.A.D. have equity in Precision Neurotek Inc. that is co-founded by the team to commercialize PtNRGrids for intraoperative mapping. S.A.D. and H.O. have competing interests not related to this work including equity in FeelTheTouch LLC. S.A.D. was a paid consultant to MaXentric Technologies. D.R.C., K.J.T, and D.A.S. have equity in Surgical Simulations, LLC. A.M.R. has an equity and is a cofounder of CerebroAI. AMR received consulting fees from Abbott Inc and Biotronik Inc.

Data and materials availability:

All data obtained in this study are either presented in the paper and supplementary materials or deposited in open database. Animal brain recording data can be accessed at OpenNeuro (https://openneuro.org/), and the human brain recording data can be accessed in Data Archive BRAIN Initiative (DABI) (https://dabi.loni.usc.edu/). Custom Matlab codes (version R2021a) in combination with open source automatic IID detection (http://www.ieeg.org) and propagating wave (https://mullerlab.github.io/) codes were used for the analyses and is available in GitHub (https://ytchoe.github.io/).

References

1. Maynard EM, Nordhausen CT, Normann RA, The Utah intracortical electrode array: a recording structure for potential brain-computer interfaces. Electroencephalography and clinical neurophysiology 102, 228–239 (1997). [PubMed: 9129578]
2. Yang T, Hakimian S, Schwartz TH, Intraoperative ElectroCorticoGraphy (ECog): indications, techniques, and utility in epilepsy surgery. Epileptic Disorders 16, 271–279 (2014). [PubMed: 25204010]
3. Penfield W, Jasper H, Epilepsy and the functional anatomy of the human brain. (1954).
4. Duffau H et al. , Contribution of intraoperative electrical stimulations in surgery of low grade gliomas: a comparative study between two series without (1985–96) and with (1996–2003) functional mapping in the same institution. Journal of Neurology, Neurosurgery & Psychiatry 76, 845–851 (2005). [PubMed: 15897509]
5. Anumanchipalli GK, Chartier J, Chang EF, Speech synthesis from neural decoding of spoken sentences. Nature 568, 493–498 (2019). [PubMed: 31019317]
6. Lachaux J-P, Axmacher N, Mormann F, Halgren E, Crone NE, High-frequency neural activity and human cognition: past, present and possible future of intracranial EEG research. Progress in neurobiology 98, 279–301 (2012). [PubMed: 22750156]
7. Mesgarani N, Cheung C, Johnson K, Chang EF, Phonetic feature encoding in human superior temporal gyrus. Science 343, 1006–1010 (2014). [PubMed: 24482117]

8. Pistohl T, Schulze-Bonhage A, Aertsen A, Mehring C, Ball T, Decoding natural grasp types from human ECoG. Neuroimage 59, 248–260 (2012). [PubMed: 21763434]
9. Kubanek J, Miller KJ, Ojemann JG, Wolpaw JR, Schalk G, Decoding flexion of individual fingers using electrocorticographic signals in humans. Journal of neural engineering 6, 066001 (2009).
10. Yanagisawa T et al. , Real-time control of a prosthetic hand using human electrocorticography signals. Journal of neurosurgery 114, 1715–1722 (2011). [PubMed: 21314273]
11. Khodagholy D et al. , NeuroGrid: recording action potentials from the surface of the brain. Nature neuroscience 18, 310–315 (2015). [PubMed: 25531570]
12. Hochberg LR et al. , Neuronal ensemble control of prosthetic devices by a human with tetraplegia. Nature 442, 164–171 (2006). [PubMed: 16838014]
13. Viventi J et al. , A conformal, bio-interfaced class of silicon electronics for mapping cardiac electrophysiology. Science translational medicine 2, 24ra22–24ra22 (2010).
14. Viventi J et al. , Flexible, foldable, actively multiplexed, high-density electrode array for mapping brain activity in vivo. Nature neuroscience 14, 1599 (2011). [PubMed: 22081157]
15. Thakor NV, Translating the brain-machine interface. Science translational medicine 5, 210ps217–210ps217 (2013).
16. Wilson GH et al. , Decoding spoken English phonemes from intracortical electrode arrays in dorsal precentral gyrus. bioRxiv, (2020).
17. Hochberg LR et al. , Reach and grasp by people with tetraplegia using a neurally controlled robotic arm. Nature 485, 372–375 (2012). [PubMed: 22596161]
18. Bensmaia SJ, Tyler DJ, Micera S, Restoration of sensory information via bionic hands. Nature Biomedical Engineering, 1–13 (2020).
19. Vargas-Irwin CE et al. , Watch, imagine, attempt: motor cortex single-unit activity reveals context-dependent movement encoding in humans with tetraplegia. Frontiers in human neuroscience 12, 450 (2018). [PubMed: 30524258]
20. Vigneau M et al. , Meta-analyzing left hemisphere language areas: phonology, semantics, and sentence processing. Neuroimage 30, 1414–1432 (2006). [PubMed: 16413796]
21. Fifer MS et al. , Simultaneous neural control of simple reaching and grasping with the modular prosthetic limb using intracranial EEG. IEEE transactions on neural systems and rehabilitation engineering 22, 695–705 (2013). [PubMed: 24235276]
22. Wang W et al. , An electrocorticographic brain interface in an individual with tetraplegia. PloS one 8, e55344 (2013). [PubMed: 23405137]
23. Acharya S, Fifer MS, Benz HL, Crone NE, Thakor NV, Electrocorticographic amplitude predicts finger positions during slow grasping motions of the hand. Journal of neural engineering 7, 046002 (2010).
24. Chiang C-H et al. , Development of a neural interface for high-definition, long-term recording in rodents and nonhuman primates. Science translational medicine 12, (2020).
25. Musk E, An integrated brain-machine interface platform with thousands of channels. Journal of medical Internet research 21, e16194 (2019). [PubMed: 31642810]
26. Sahasrabuddhe K et al. , The Argo: a high channel count recording system for neural recording in vivo. Journal of Neural Engineering 18, 015002 (2021).
27. Ganji M et al. , Selective formation of porous Pt nanorods for highly electrochemically efficient neural electrode interfaces. Nano letters 19, 6244–6254 (2019). [PubMed: 31369283]
28. Liao F-J. (Google Patents, 2007).
29. Shirai H, Inoue M, Hashimoto S. (Google Patents, 2006).
30. Uguz I et al. , Autoclave sterilization of PEDOT: PSS electrophysiology devices. Advanced healthcare materials 5, 3094–3098 (2016). [PubMed: 27885829]
31. Petersen CC, The functional organization of the barrel cortex. Neuron 56, 339–355 (2007). [PubMed: 17964250]
32. Keller A, in The barrel cortex of rodents. (Springer, 1995), pp. 221–262.
33. Ray S, Crone NE, Niebur E, Franaszczuk PJ, Hsiao SS, Neural correlates of high-gamma oscillations (60–200 Hz) in macaque local field potentials and their potential implications in electrocorticography. Journal of Neuroscience 28, 11526–11536 (2008). [PubMed: 18987189]

34. Liguz-Lecznar M, Skangiel-Kramska J, Vesicular glutamate transporters VGLUT1 and VGLUT2 in the developing mouse barrel cortex. International journal of developmental neuroscience 25, 107–114 (2007). [PubMed: 17289331]
35. Neafsey E et al. , The organization of the rat motor cortex: a microstimulation mapping study. Brain research reviews 11, 77–96 (1986).
36. Fonoff ET et al. , Functional mapping of the motor cortex of the rat using transdural electrical stimulation. Behavioural brain research 202, 138–141 (2009). [PubMed: 19447290]
37. Romstöck J, Fahlbusch R, Ganslandt O, Nimsky C, Strauss C, Localisation of the sensorimotor cortex during surgery for brain tumours: feasibility and waveform patterns of somatosensory evoked potentials. Journal of Neurology, Neurosurgery & Psychiatry 72, 221–229 (2002). [PubMed: 11796773]
38. Cedzich C, Taniguchi M, Schäfer S, Schramm J, Somatosensory evoked potential phase reversal and direct motor cortex stimulation during surgery in and around the central region. Neurosurgery 38, 962–970 (1996). [PubMed: 8727822]
39. Haseeb A et al. , Young patients with focal seizures may have the primary motor area for the hand in the postcentral gyrus. Epilepsy research 76, 131–139 (2007). [PubMed: 17723289]
40. Duffau H, Sichez JP, Lehéricy S, Intraoperative unmasking of brain redundant motor sites during resection of a precentral angioma: evidence using direct cortical stimulation. Annals of neurology 47, 132–135 (2000). [PubMed: 10632114]
41. Wood CC et al. , Localization of human sensorimotor cortex during surgery by cortical surface recording of somatosensory evoked potentials. Journal of neurosurgery 68, 99–111 (1988). [PubMed: 3275756]
42. Bleichner M et al. , The effects of blood vessels on electrocorticography. Journal of neural engineering 8, 044002 (2011).
43. Balzamo E, Marquis P, Chauvel P, Regis J, Short-latency components of evoked potentials to median nerve stimulation recorded by intracerebral electrodes in the human pre-and postcentral areas. Clinical neurophysiology 115, 1616–1623 (2004). [PubMed: 15203062]
44. Pfurtscheller G, Graimann B, Huggins JE, Levine SP, Schuh LA, Spatiotemporal patterns of beta desynchronization and gamma synchronization in corticographic data during self-paced movement. Clinical neurophysiology 114, 1226–1236 (2003). [PubMed: 12842719]
45. Shibasaki H, Hallett M, What is the Bereitschaftspotential? Clinical neurophysiology 117, 2341–2356 (2006). [PubMed: 16876476]
46. Pfurtscheller G, Neuper C, Event-related synchronization of mu rhythm in the EEG over the cortical hand area in man. Neuroscience letters 174, 93–96 (1994). [PubMed: 7970165]
47. Rubino D, Robbins KA, Hatsopoulos NG, Propagating waves mediate information transfer in the motor cortex. Nature neuroscience 9, 1549–1557 (2006). [PubMed: 17115042]
48. Muller L et al. , Rotating waves during human sleep spindles organize global patterns of activity that repeat precisely through the night. Elife 5, e17267 (2016). [PubMed: 27855061]
49. So EL, Integration of EEG, MRI, and SPECT in localizing the seizure focus for epilepsy surgery. Epilepsia 41, S48–S54 (2000).
50. Chari A, Thornton RC, Tisdall MM, Scott RC, Microelectrode recordings in human epilepsy: A case for clinical translation? Brain Communications, (2020).
51. Taplin AM et al. , Intraoperative mapping of expressive language cortex using passive real-time electrocorticography. Epilepsy & Behavior Case Reports 5, 46–51 (2016). [PubMed: 27408802]
52. Jacobs J et al. , Value of electrical stimulation and high frequency oscillations (80–500 Hz) in identifying epileptogenic areas during intracranial EEG recordings. Epilepsia 51, 573–582 (2010). [PubMed: 19845730]
53. Janca R et al. , Detection of interictal epileptiform discharges using signal envelope distribution modelling: application to epileptic and non-epileptic intracranial recordings. Brain topography 28, 172–183 (2015). [PubMed: 24970691]
54. Donos C, Mîndruţă I, Ciurea J, Mălîia MD, Barborica A, A comparative study of the effects of pulse parameters for intracranial direct electrical stimulation in epilepsy. Clinical Neurophysiology 127, 91–101 (2016). [PubMed: 25910851]

55. McIntyre CC, Grill WM, Finite element analysis of the current-density and electric field generated by metal microelectrodes. Annals of biomedical engineering 29, 227–235 (2001). [PubMed: 11310784]

56. Iwamoto K, in Novel Patterning Technologies for Semiconductors, MEMS/NEMS and MOEMS 2020. (International Society for Optics and Photonics, 2020), vol. 11324, pp. 1132405.

57. Davis ZW, Muller L, Martinez-Trujillo J, Sejnowski T, Reynolds JH, Spontaneous travelling cortical waves gate perception in behaving primates. Nature 587, 432–436 (2020). [PubMed: 33029013]

58. Inoue T, Shimizu H, Nakasato N, Kumabe T, Yoshimoto T, Accuracy and limitation of functional magnetic resonance imaging for identification of the central sulcus: comparison with magnetoencephalography in patients with brain tumors. Neuroimage 10, 738–748 (1999). [PubMed: 10600419]

59. Dewan MC et al. , Global neurosurgery: the current capacity and deficit in the provision of essential neurosurgical care. Executive Summary of the Global Neurosurgery Initiative at the Program in Global Surgery and Social Change. Journal of neurosurgery 130, 1055–1064 (2018).

60. Simeral JD et al. , Home use of a percutaneous wireless intracortical brain-computer interface by individuals with tetraplegia. IEEE Transactions on Biomedical Engineering, (2021).

61. Lauer SM, Schneeweiß U, Brecht M, Ray S, Visualization of cortical modules in flattened mammalian cortices. JoVE (Journal of Visualized Experiments), e56992 (2018).

62. Kaiju T, Inoue M, Hirata M, Suzuki T, High-density mapping of primate digit representations with a 1152-channel μECoG array. Journal of Neural Engineering 18, 036025 (2021).

63. Chiang C-H et al. , Flexible, high-resolution thin-film electrodes for human and animal neural research. Journal of neural engineering (2021).

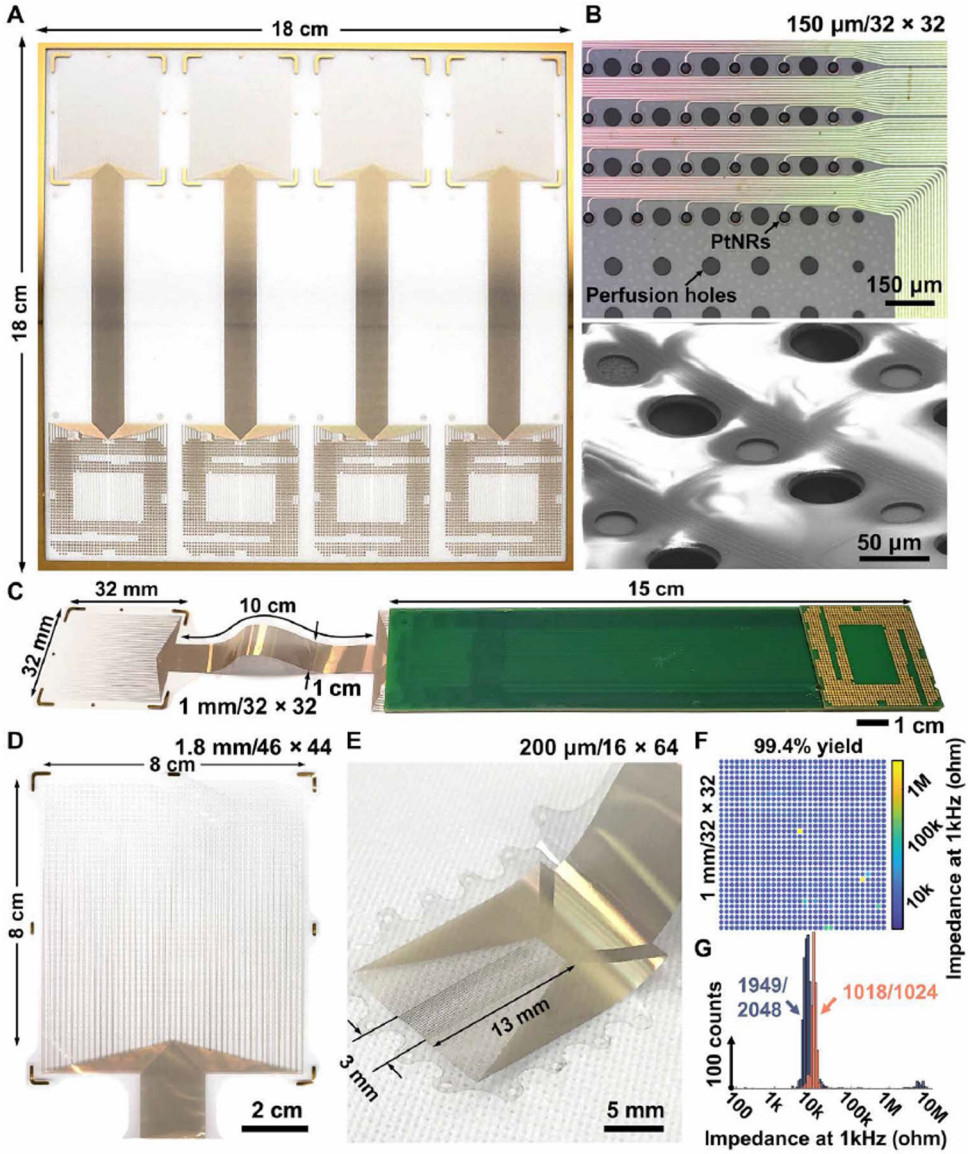

Fig. 1. Multi-thousand channel PtNRGrids ECoG arrays.

(A) Scalable and large-area fabrication of electrode arrays on 18 × 18 cm^2 glass substrates. Microscale features of PtNRs contacts, metal leads, and perfusion holes shown by (B) optical (top) and electron microscope images (bottom). (C) A 1024 channel electrode bonded on the extender PCB that is compatible with CPU LGA sockets. Reconfigurable electrode designs depending on the target placement on the human brain with a sensing area of (C) 32 × 32 mm^2 (1024 channel), (D) 8 × 8 cm^2 (2048 channel), and (E) 3 × 13 mm^2 (1024 channel). (F) Spatial mapping and (G) histogram of the impedance magnitude at 1 kHz for the 1024 and 2048 channel electrode. 1024 and 2048 channel electrodes had 1 kHz impedance magnitude of 11 ± 2 kΩ and 8 ± 4 kΩ with a yield up to 99.4 and 95.2%, respectively.

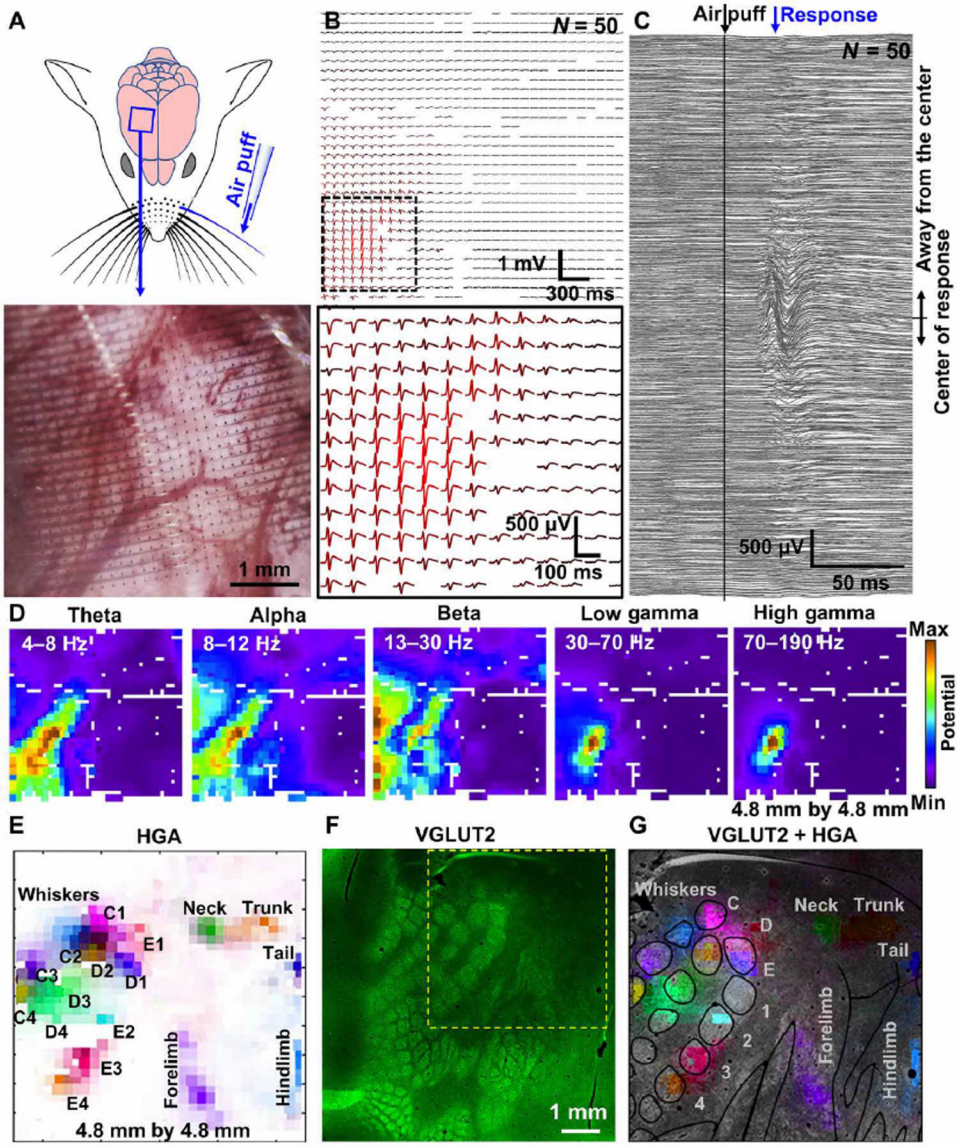

Fig. 2. PtNR multi-thousand channel ECoG grids record somatotopic functional cortical columns with sub-millimeter resolution.

(A) Schematic of the rat brain implanted with 1024 channels, 4.8 mm × 4.8 mm array, and the air-puff stimulation of individual whiskers. The lower image shows the magnified microscope image of the electrode on the rat barrel cortex. (B) E4 whisker stimulation-evoked ECoG recordings (N=50, raw). (C) Stimulation locked response of all channels. (D) Spatial mapping of neural wave amplitude filtered at different frequency windows. (E) Spatial mapping of high gamma activity recorded by the high-density PtNRGrid. Each label indicates the positions stimulated with air-puff. (F) VGLUT2 immunostaining of the rat barrel cortex. The electrode implantation location is marked with the yellow dotted box. (G) HGA superimposed on top of the histology image.

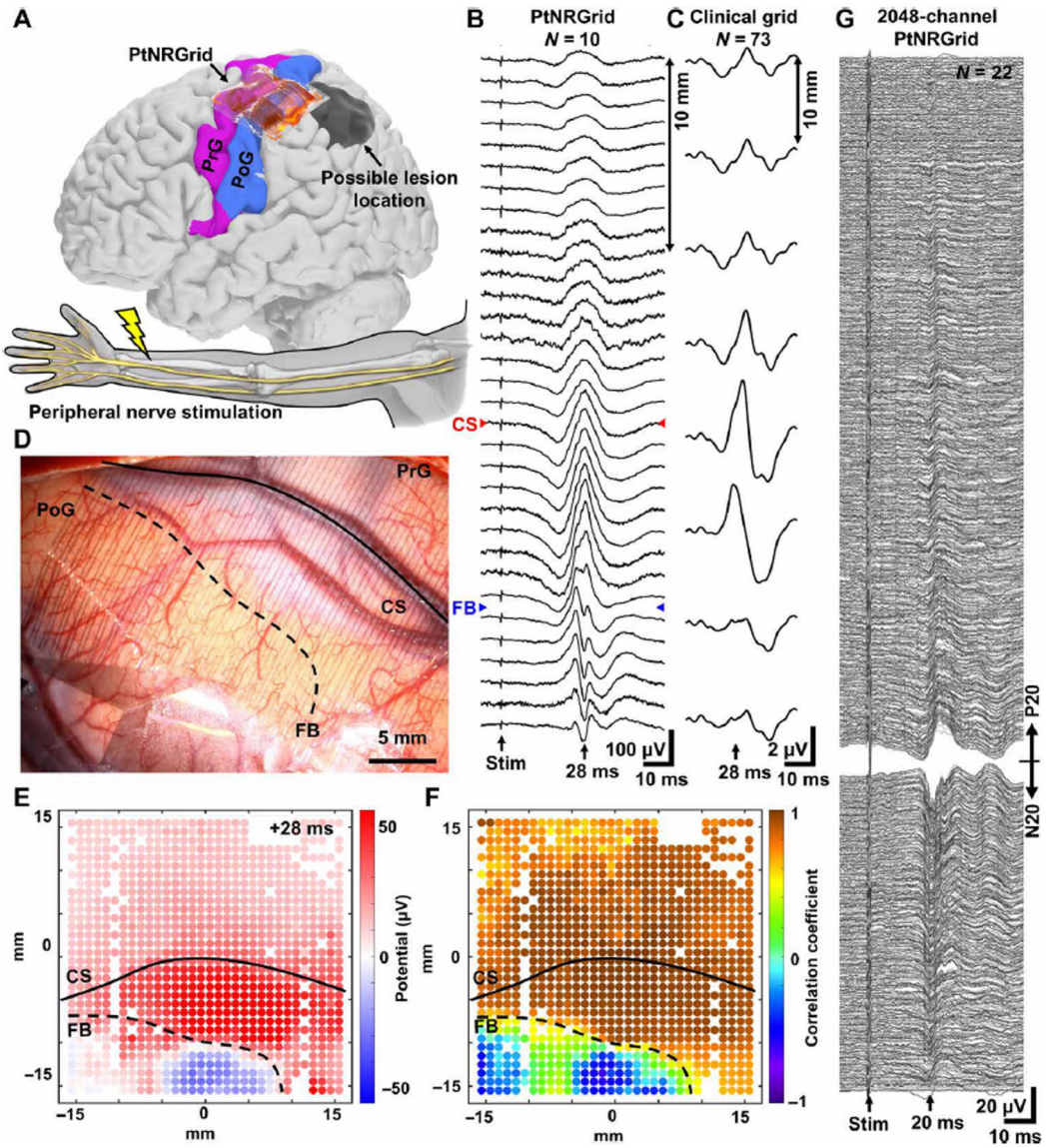

Fig. 3. Mapping the curvilinear nature of the functional sensory/motor regions in the human brain with millimeter resolution.

(A) Reconstructed model of the patient's brain and the electrode implantation locations. Electrodes were implanted near the hand region, and the peripheral nerve was electrically stimulated. Somatosensory evoked potential (SSEP) waveforms along a line across the central sulcus (CS) and M1-S1 functional boundary (FB) recorded with (B) 32×32 PtNRGrid with 1 mm spacing and (C) 2×8 clinical grid with 10 mm spacing. (D) Implantation picture of the electrodes near the hand region. (E) 1024-channels potential mapping of the stim-evoked waves 28 ms after the stimulation (as opposed to 20 ms due to distortion from brain lesion as shown in panels (B) and (C). (F) Correlation coefficient mapping with respect to the waveforms measured with respect to the channel in the center of the grid. (G) Human brain SSEPs from 2048 channel PtNRGrid. Channels are sorted according to the peak potential amplitude and polarity at 20 ms after the stimulation, and channels with high contact impedance were excluded from the plot.

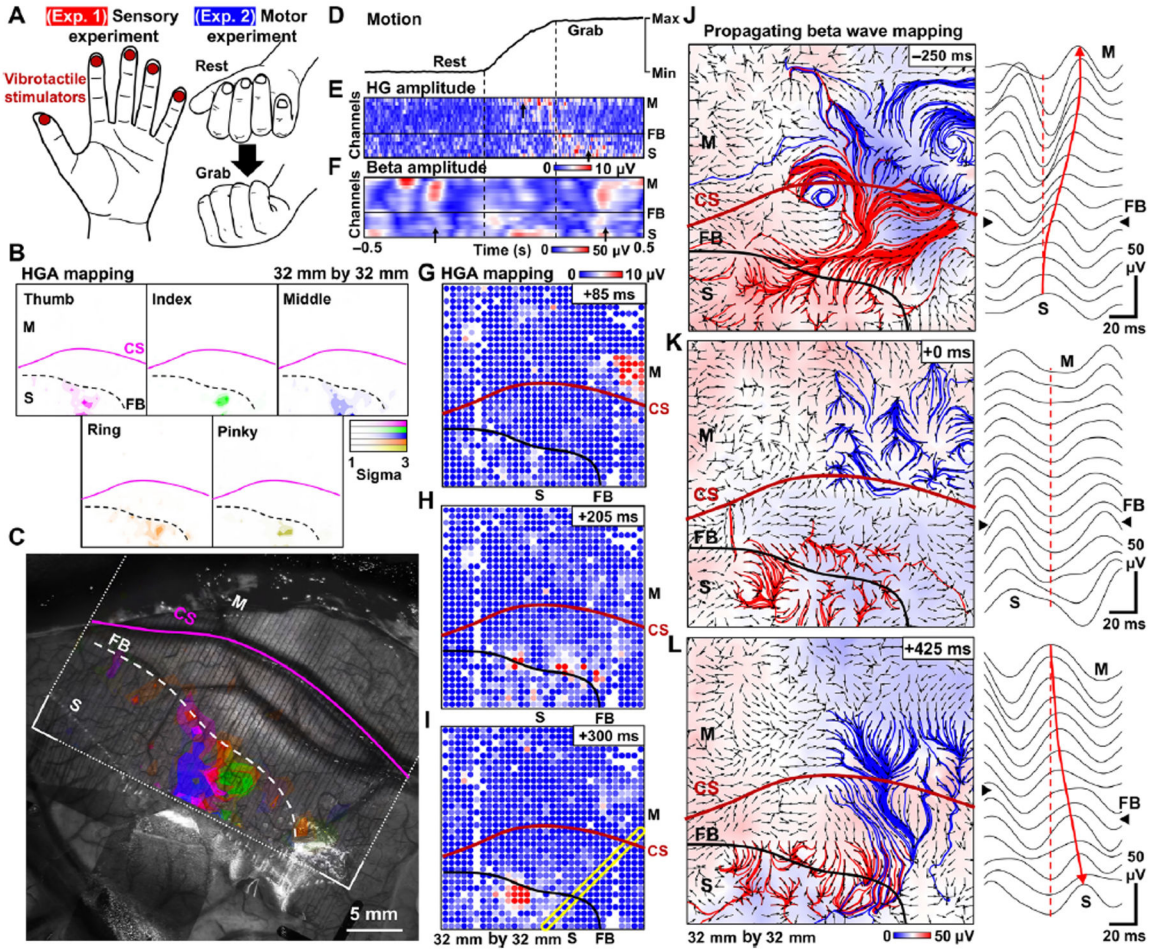

Fig. 4. Functional mapping with millimeter resolution: PtNRGrid records detailed sensory and motor spatiotemporal dynamics in humans.

(A) Schematics of the sensory and motor experiments. For sensory experiment, individual fingers were stimulated by vibrotactile stimulation in sequence with 1 s stimulation at 2 s intervals. For the motor experiment, the patient was asked to perform a grasping task. (B) Spatial mapping of high gamma activity (HGA) of individual fingers in response to vibrotactile stimulations. (C) Overlay plot of HGA sensory responses for individual fingers superimposed on top of a photo of the surface of the patient's brain. (D) Motion of the hand recorded with the bending sensor. The amplitude of (E) HGA and (F) Beta activity of channels selected along the yellow diagonal rectangle in (I) plotted over a 1 s time window during the motion. Spatial mapping of HGA over three different time points during the hand grabbing motion. (G) Initially localized HGA appears on the motor region, (H) then both the motor and sensory region show HGA, and (I) eventually the HGA only appears on the sensory region. Propagating beta waves and waveforms across the CS in the (J) planning stage of the motion, (K) during the motion, and (L) after the completion of motion. The red and blue streamlines originate from sensory and motor cortex, respectively. The background color represents the amplitude of the beta wave potential, and the arrows indicates the propagating direction of the beta waves. Right panel plots are raw waveforms for the yellow box in (I) around the timestamps of (J)-(L).

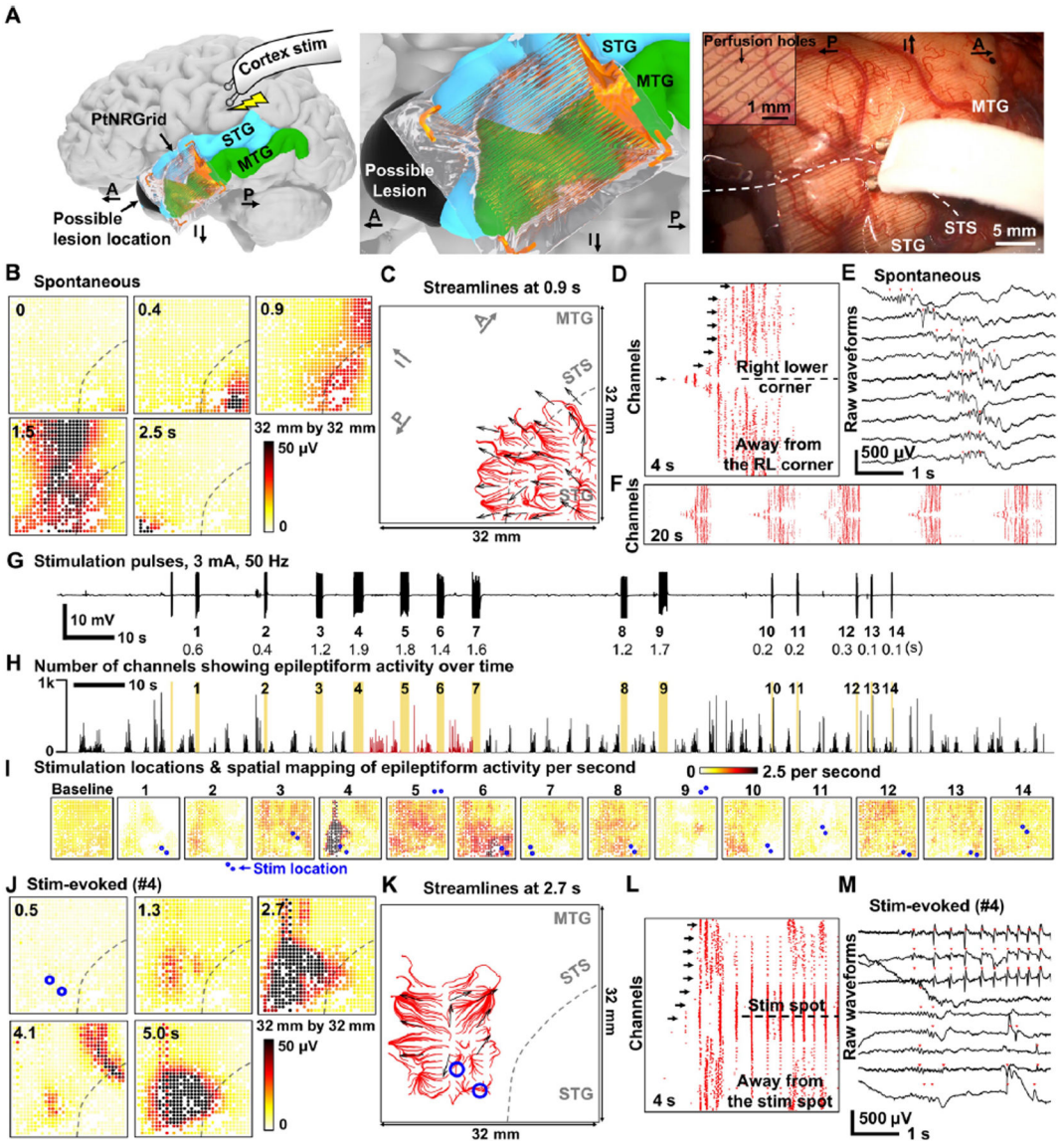

Fig. 5. Pathological mapping with millimeter resolution: PtNRGrids reveal detailed spatiotemporal dynamics of spontaneous and stimulated epileptiform discharges from an epilepsy patient.

(A) (Left) Reconstructed model of electrode placement on the temporal lobe of the patient's brain, and the schematics of charge-balanced bi-phasic direct current stimulation with the bipolar (Ojemann) probe. (Middle) Magnified model near the electrode. (Right) Photo showing the cortical tissues directly being stimulated through the electrode. Inset is a magnified image showing the 0.5 mm diameter perfusion holes that are distributed at a 1mm pitch on the electrode allowing direct current stimulation at any point on the grid. Positions of the superior temporal sulcus (STS), superior temporal gyrus (STG), and middle temporal gyrus (MTG) are marked on the photo. Anatomical orientation arrows indicate anterior (A), posterior (P), and inferior (I). **(B)-(F)** Spontaneous epileptiform discharges. (B) Spatial mapping of the 10–59 Hz spontaneous brain wave amplitude. Location of STS is marked with dotted lines. (C) Streamlines plot at 0.9 s depicting the spontaneous

propagating wave together with the vectors indicating the direction of propagating waves. Automatically detected epileptiform discharges for all channels in (D) 4s and (F) 20s time windows. (E) Raw waveforms selected from arrow marked channels of (D). The channels are sorted according to the distance from the right lower corner of the electrode; the channel in the midline is closest to the lower right corner. (G) Time course and recordings of the stimulation pulse artifacts for time-locking with evoked response. The stimulation sequence number and duration of stimulation time is indicated below the waveforms. (H) Number of channels showing epileptiform discharges over time. The yellow color indicates the stimulation time points, and the red colored regions mark significant enhancement in epileptiform discharges detection for stimulations number 4, 5 and 6 ($p < .001$). (I) Spatial mapping of epileptiform discharge rate after each stimulation trial. Stimulation locations on or near the electrode are indicated by pair of blue dots for the 14 stimulation trials. **(J)-(M)** Stimulation evoked epileptiform discharges, similar to (B)–(F). (J) Spatial mapping of the 10–59 Hz stim-evoked brain wave amplitude. (K) Streamlines plot at 2.7 s depicting the stim-evoked propagating wave together with the vectors indicating the direction of propagating waves. (L) Automatically detected epileptiform discharges for all channels in a 4 s time window. The channels are sorted according to the distance from the stimulation point. (M) Raw waveforms selected from arrow marked channels of (L). Propagating waves for (C) spontaneous epileptiform discharge and (K) stimulation-evoked epileptiform discharge. The red streamlines for (C) originate from the right lower corner while those for (K) originates near the stimulation location. The blue circles in (K) are the bipolar stimulator contact points on the cortex.